J. Mech. Phys. Solids 186 (2024) 105590

Contents lists available at ScienceDirect

Journal of the Mechanics and Physics of Solids

journal homepage: www.elsevier.com/locate/jmps

Third-order exceptional points and frozen modes in planar elastic laminates

Ariel Fishman, Guy Elbaz, T. Venkatesh Varma, Gal Shmuel *

Faculty of Mechanical Engineering, Technion–Israel Institute of Technology, Haifa 32000, Israel

ARTICLE INFO

Keywords:
Exceptional points
Non-Hermitian physics
Composites
wave propagation
Bloch Floquet waves
Frozen modes
Metamaterials

ABSTRACT

Exceptional points (EPs) are degeneracies of two or more natural modes of open systems, which lead to unusual wave phenomena. Despite the robustness against imperfections of spatial EPs, they are less studied relative to temporal EPs, particularly in elastodynamics. However, elastic waves exhibit features not found in sound and light, which have proven useful for forming spatial EPs. Here, we harness these features to tune the coalescence of three eigenmodes in the Bloch spectrum of planar elastic laminates. We show that these third-order EPs give rise to *axially frozen modes*: anomalous transmitted waves with zero axial group velocity and finite transmittance. These modes, which were first reported in optics and required three-dimensional laminates, are achieved here in a planar setting thanks to elastodynamics tensorial structure, and expand the toolbox for elastic wave shaping.

1. Introduction

Open systems, which are described by non-Hermitian operators, admit degenerate states at which two or more of their eigenmodes coalesce (Moiseyev, 2011; Kato, 1966; Ashida et al., 2020; El-Ganainy et al., 2019; Srikantha Phani, 2022; Bigoni and Kirillov, 2019). These degeneracies, termed *exceptional points* (EPs) (Miri and Alù, 2019; Midya et al., 2018), present exotic wave phenomena, such as anisotropic transmission (Lin et al., 2011; Longhi, 2011; Elbaz et al., 2022), hypersensitivity (Wiersig, 2014; Djorwe et al., 2019; Shmuel and Moiseyev, 2020; Kononchuk et al., 2022), and enrich coherent perfect absorption (Sweeney et al., 2019; Wang et al., 2021; Goldstein and Shmuel, 2023), thus serve as tool for metamaterial design (Achilleos et al., 2017; Assouar et al., 2018; Katsantonis et al., 2020; Fang et al., 2021; Wang and Amirkhizi, 2022; Gupta et al., 2023).

Most works are on temporal EPs which form when two (or more) resonance frequencies coalesce. These works incorporate gain and loss that are often balanced to form parity-time symmetry for temporal stability (Longhi, 2017; Rosa et al., 2021; Fang et al., 2022; Özdemir et al., 2019; El-Ganainy et al., 2018; Feng et al., 2017; Fleury et al., 2014, 2015; Christensen et al., 2016; Merkel et al., 2018; Shi et al., 2016; Domínguez-Rocha et al., 2020).

Spatial EPs forming in the complex wavevector space at real frequencies have received less attention, particularly in elastodynamics (Mokhtari et al., 2019), despite their robustness against imperfections (Tuxbury et al., 2022). However, elastic waves exhibit features not found in sound and light waves (Chaplain et al., 2020), which can be harnessed to design spatial EPs.

To appreciate this, consider the ubiquitous scenario of isotropic media, in which case acoustic waves are longitudinal, electromagnetic waves are transverse, while only elastic waves exhibit both polarizations (Psiachos and Sigalas, 2019). Lustig et al. (2019) recognized that this distinctive coexistence of polarizations in elastodynamics offers a simpler alternative to design spatial EPs and access some of their unique phenomena, instead of judicially designing gain and loss. By revisiting the classical problem

* Corresponding author.
E-mail address: meshmuel@technion.ac.il (G. Shmuel).

https://doi.org/10.1016/j.jmps.2024.105590
Received 3 October 2023; Received in revised form 16 January 2024; Accepted 23 February 2024
Available online 28 February 2024

of in-plane waves in two alternating elastic isotropic materials, they showed that the energy transfer between the polarizations at material interfaces can be tuned to cause the coalescence of the laminate's two Bloch modes (EP2). They further showed that these spatial EPs give rise to anomalous energy transport in the canonical scattering problem, particularly negative refraction. We reemphasize that these EPs form in the Bloch spectrum, and thus the work of Lustig et al. (2019) belongs to the emerging field of physics of non-resonant EPs (Sweeney et al., 2019; Tuxbury et al., 2021), distinct from mainstream research on resonant EPs.

Here, we analytically establish the coalescence of *three* natural modes (EP3) in the Bloch spectrum of periodic elastic laminates composed of two anisotropic materials, and investigate the implications of these higher-order degeneracies. Although wave propagation in periodic anisotropic elastic layers is a classical problem (Braga and Herrmann, 1992; Nayfeh, 1991) that is still being studied (Guo et al., 2023), this is the first observation of EP3 in their spectrum.

Our analytical analysis is motivated by the pioneering work of Figotin and Vitebskiy (2003), who derived the conditions for EP3 in the Bloch spectrum of *dielectric* laminates. They further showed that these EPs may cause obliquely incident light to refract through the laminate with nearly unity transmittance and large amplitude, while having vanishing group velocity in the lamination direction. Owing to the latter property, Figotin and Vitebskiy (2003) termed these modes *axially frozen modes*; their discovery paved the way for a series of works on electromagnetic frozen modes and their applications (Nada et al., 2021; Tuxbury et al., 2022; Apaydin et al., 2012; Zamir-Abramovich et al., 2023; Tuxbury et al., 2021; Gan et al., 2019).

In the sequel, we derive the necessary conditions for non-resonant EP3 in the Bloch spectrum of planar elastic laminates, using a simpler approach than the one taken by Figotin and Vitebskiy (2003). Importantly, we show that it is possible to design EP3 and excite frozen modes in planar elastic laminates, in contrast with dielectric laminates, where a three-dimensional setting is necessary (see section II.B in the paper of Figotin and Vitebskiy, 2003). This fundamental and useful difference results from the tensorial richness in elastodynamics, relative to electrodynamics. Quantitatively, the former is governed by a fourth-order (elasticity) tensor field, while the latter is by a second-order (permittivity) tensor field. It is this tensorial difference that enables the additional wave polarizations and couplings mentioned earlier.

To demonstrate that EP3 indeed forms in our setting, we select exemplary anisotropic materials according to our derived conditions; and use them as the constituents of a designated laminate. To illustrate the implications of this degeneracy on elastic scattering, we revisit the exact solution of the canonical transmission problem of monochromatic plane waves incident on a semi-infinite laminate (Joseph and Craster, 2015), and analyze the resultant scattering. Using our design parameters, we exemplify how the transmittance near EP3 is finite, in spite of the fact that the group velocity of the transmitted Bloch wave vanishes, thereby giving rise to elastic axially frozen modes. This can occur only if the energy density diverges at the same rate that the group velocity decays, as our analysis confirms. We further demonstrate how the transmittance near the EP3 significantly depends on the properties of the incoming wave; and show that by shaping the incoming wave, it is possible to achieve unity transmittance at the EP3.

To support our analytical calculations, we carry out full-field finite elements simulations of the transmission problem using the commercial code COMSOL. We find that the transmittance extracted from the computational simulations agree with our analytical calculations. Finally, we illustrate the hallmark of non-Hermitian degeneracy, namely, the tendency of the eigenmodes to coalesce as the incoming wave frequency approaches the EP3 frequency.

Before we outline the structure of this paper, we note that our theoretical model is an idealization of what we expect from its experimental realization. As such, the frozen modes would be limited to some extent by the practical deviations from the idealized settings, such as material defects, finiteness of the specimen, nonlinear effects (see recent efforts to analyze nonlinear EPs by Suntharalingam et al., 2023 and Benzaouia et al., 2022), etc. Nevertheless, spatial EPs are robust against imperfections that cause variation in the wavenumber (Tuxbury et al., 2022; Gan et al., 2019; Li et al., 2017), such as imperfections in the boundary conditions or geometry.

Our analysis is presented as follows. Section 2 summarizes the equations that govern in-plane waves in periodic laminates, together with the transfer matrix method to solve them. In Section 3, we first derive the algebraic conditions for the emergence of EP3 in the Bloch spectrum of the laminate. Subsequently, we relate these conditions to the symmetries of the materials that compose the laminate. We show that it is sufficient to include one anisotropic material (subjected to certain conditions) in the unit cell, in order for EP3 to form. We conclude Section 3 with some important properties of the energy flux in the laminate. Section 4 contains our parametric examples of designated laminates with spectral EP3; analysis of the canonical transmission problem with elastic frozen modes of unity transmittance; and computational simulations that support our analytical calculations. We finalize this paper with a summary of our main results and conclusions.

2. In-plane waves in periodic laminates

Solutions to the problem of in-plane waves in elastic laminates made of isotropic- (Brekhovskikh, 1960; Lowe, 1995; Adams et al., 2009) and anisotropic (Nayfeh, 1995) materials are well-known. For completeness and to introduce our notation, these solutions are summarized next using Stroh's formulation (Stroh, 1962; Braga and Herrmann, 1992).

We consider an infinite laminate made of two materials, denoted by a and b, that are repeated periodically in the x_1 direction. We denote the thickness of material a (b) by $h^{(a)}$ ($h^{(b)}$), such that the thickness of the unit cell is $h = h^{(a)} + h^{(b)}$ (Fig. 1(a)). The laminate undergoes time-harmonic motion in the $\left(x_1, x_2\right)$ plane in the form of $\boldsymbol{u} = \hat{\boldsymbol{u}}\left(x_1\right) e^{i\left(k_2 x_2 - \omega t\right)}$, where $\boldsymbol{u}$ is the displacement field, k_2 is the transverse wavenumber and ω is the angular frequency; here and henceforth, overhead hat denotes functions of x_1. The objective is to determine the form of $\hat{\boldsymbol{u}}\left(x_1\right)$ at prescribed values of ω (say, owing to a time-harmonic source) and k_2 (when the

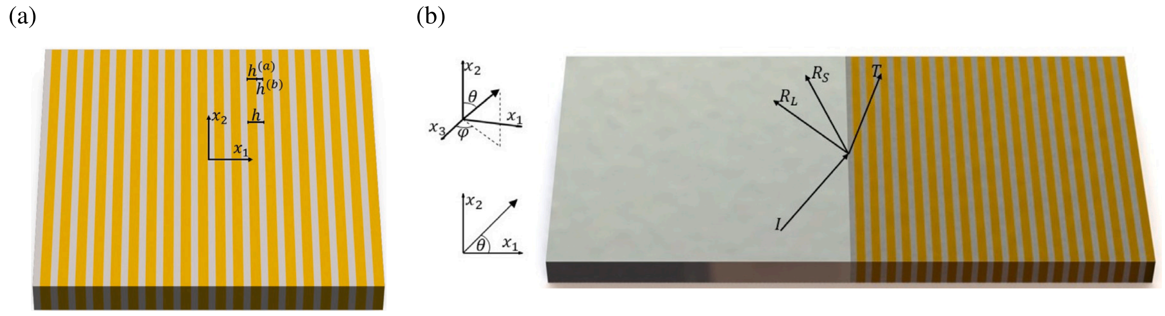

Fig. 1. (a) Portion of an infinite laminate made of materials a and b, repeated periodically in the x_1 direction. The unit cell thickness is h. (b) Semi-infinite laminate connected at $x_1 = 0$ to a homogeneous half-space, from which an incoming wave with an amplitude I propagates in an angle θ_i towards the interface. The incident, transmitted and reflected pressure and shear waves are denoted by I, T, R_L and R_S, respectively. The upper (lower) 3D (2D) coordinate system depicts a wavevector that propagates with (without) horizontal angle φ and vertical angle θ.

incident wave encounters a plane whose normal is x_1, as in the canonical scattering problem). To this end, we solve the equation of linear momentum

$$\nabla \cdot \boldsymbol{\sigma} = \rho \ddot{\boldsymbol{u}}, \tag{1}$$

where ρ is the mass density, and the stress $\boldsymbol{\sigma}$ is related to $\boldsymbol{u}$ through the constitutive equation

$$\boldsymbol{\sigma} = \mathbf{C} : \left(\nabla \boldsymbol{u} + \nabla \boldsymbol{u}^{\mathrm{T}}\right)/2, \tag{2}$$

where $\mathbf{C}$ is the elasticity tensor, which may be anisotropic. Owing to the periodicity of the laminate, ρ and $\mathbf{C}$ are h-periodic in x_1. After some manipulation (see Appendix A), Eq. (1) can be written as

$$\frac{\partial}{\partial x_1} \mathsf{s}\left(x_1\right) = \mathsf{A}\left(x_1\right) \mathsf{s}\left(x_1\right), \tag{3}$$

where

$$\mathsf{s}\left(x_1\right) = \begin{pmatrix} \hat{u}_1 & \hat{u}_2 & \hat{\sigma}_{11} & \hat{\sigma}_{21} \end{pmatrix}^{\mathsf{T}}, \tag{4}$$

and the propagator matrix A (whose components are given in Appendix A) is a function of k_2, ω and the mechanical properties of each layer. In the sequel, we will link the material symmetries to the properties of A and, in turn, the formation of EP3. The so-called state vector s comprises quantities that are continuous throughout the medium, and in particular at interfaces between the layers. Using these continuity conditions and the fact that A is piecewise-constant, we can integrate Eq. (3) over a representative unit cell, and relate the state vector at $x_1 = 0$ and $x_1 = h$ via

$$\mathsf{s}(h) = \mathsf{T}\mathsf{s}(0), \tag{5}$$

where the transfer matrix T is

$$\mathsf{T} := \mathsf{T}^{(b)}\mathsf{T}^{(a)} = e^{\mathsf{A}^{(b)}h^{(b)}} e^{\mathsf{A}^{(a)}h^{(a)}}, \tag{6}$$

and $\mathsf{A}^{(n)}$ is the value of A at layer n. The values of the state vector at the two ends of the periodic cell are also related via the Bloch–Floquet theorem

$$\mathsf{s}\left(x_1\right) = \mathsf{s}_{\mathrm{p}}(x_1)e^{i\kappa x_1},\ \mathsf{s}_{\mathrm{p}}(x_1 + h) = \mathsf{s}_{\mathrm{p}}(x_1), \tag{7}$$

where κ is the Bloch wavenumber, hence

$$\mathsf{s}(h) = e^{i\kappa h}\mathsf{s}(0). \tag{8}$$

Eqs. (5)–(8) together constitute the eigenvalue problem

$$[\mathsf{T} - \Lambda \mathrm{I}]\,\mathsf{s}(0) = 0 \tag{9}$$

for the (exponent of the) Bloch wavenumbers $\Lambda := e^{i\kappa h}$ and eigenmodes. Eq. (9) dictates the *dispersion relation* $\omega(\kappa)$ between the frequency ω and the Bloch wavenumber κ. We recall that owing to the periodicity of the medium, if κ is a solution, then so is $\kappa h + 2\pi m$ for any integer m; therefore, one can extract the dispersion curves at any κ from the curves in the first Brillouin zone $-\pi/h \leq \kappa \leq \pi/h$. In certain cases, the spectrum exhibits axial symmetry by virtue of the properties of the constituents, and then it is sufficient to evaluate the spectrum for $0 \leq \kappa \leq \pi/h$ (Lee and Yang, 1973; Guo et al., 2023); we will analyze the conditions under which this symmetry breaks down.

3. Relevant properties of the Bloch spectrum

3.1. Characteristic polynomial and triple roots

Eq. (9) delivers the quartic characteristic polynomial

$$p(\Lambda) = \Lambda^4 - I_1\Lambda^3 + I_2\Lambda^2 - I_3\Lambda + I_4 = 0, \tag{10}$$

where $\{I_k\}$ are the invariants of the transfer matrix, given by

$$I_1 = \mathrm{tr}(\mathsf{T}), I_2 = \frac{1}{2}\left[\mathrm{tr}(\mathsf{T})^2 - \mathrm{tr}\left(\mathsf{T}^2\right)\right], I_3 = \frac{1}{6}\left[\mathrm{tr}(\mathsf{T})^3 - 3\mathrm{tr}\left(\mathsf{T}^2\right)\mathrm{tr}(\mathsf{T}) + 2\mathrm{tr}\left(\mathsf{T}^3\right)\right], I_4 = \det(\mathsf{T}). \tag{11}$$

The characteristic polynomial can be factored into a product of the form

$$p(\Lambda) = \left(\Lambda - \Lambda_1\right)\left(\Lambda - \Lambda_2\right)\left(\Lambda - \Lambda_3\right)\left(\Lambda - \Lambda_4\right). \tag{12}$$

Near EP3, there exists an eigenvalue whose algebraic multiplicity is 3, the dispersion relation can be approximated as

$$\omega - \omega_{\mathrm{EP3}} \sim \left(\kappa - \kappa_{\mathrm{EP3}}\right)^3, \tag{13}$$

where $\left(\omega_{\mathrm{EP3}}, \kappa_{\mathrm{EP3}}\right)$ are the frequency–wavenumber pair forming EP3. Accordingly, EP3 is also a stationary inflection point, at which

$$\frac{\partial\omega}{\partial\kappa} = 0,\ \frac{\partial^2\omega}{\partial\kappa^2} = 0,\ \frac{\partial^3\omega}{\partial\kappa^3} \neq 0, \tag{14}$$

where the rest of the parameters of the problem are taken as fixed when evaluating the partial derivatives, including k_2. Eq. (13) explains the robustness against small variations in κ near EP3; conversely, the inverse equation states that small variations from κ_{EP3} are proportional to $(\omega - \omega_{\mathrm{EP3}})^{1/3}$, which explains the high sensitivity to perturbations in the frequency.

From the general formula for the roots of quartic equations, the necessary algebraic conditions on the invariants of the quartic characteristic polynomial to have at least a triple root are

$$\Delta_0 = I_2^2 - 3I_1I_3 + 12I_4 = 0, \tag{15}$$

$$\Delta_1 = 2I_2^3 - 9I_1I_2I_3 + 27I_1^2I_4 + 27I_3^2 - 72I_2I_4 = 0. \tag{16}$$

Note that conditions (15)–(16) are applicable for characteristic polynomials with imaginary coefficients. These equations cannot be satisfied by any laminate, as we explain next.

3.2. Relations with material symmetries

The symmetries of the materials that comprise the periodic cell determine the coefficients of the characteristic polynomial, and, in turn, the possible degeneracies of the spectrum. When all the layers are made of isotropic materials and $k_2 \in \mathbb{R}$ (i.e., the wave does not decay in the x_2 direction, as in the canonical scattering problem), the coefficients are real and satisfy the so-called reversibility property (Romeo and Luongo, 2002; Lustig et al., 2019; Mokhtari et al., 2020)

$$I_1 = I_3, I_4 = \det\mathsf{T} = 1. \tag{17}$$

To see that $\det\mathsf{T}$ is 1, we note that $\mathrm{tr}\,\mathsf{A} = 0$ for isotropic layers [in this case α_2 is zero in Eq. (A.5)], and hence

$$\det\mathsf{T} = \det\left(e^{\mathsf{A}^{(b)}h^{(b)}}e^{\mathsf{A}^{(a)}h^{(a)}}\right) = e^{\mathrm{tr}\mathsf{A}^{(b)}h^{(b)}}e^{\mathrm{tr}\mathsf{A}^{(a)}h^{(a)}} = e^0e^0 = 1. \tag{18}$$

The reversibility property constrains the eigenvalues to appear in two reciprocal pairs[1], such that if Λ_1 and Λ_2 are roots of $p(\Lambda)$, then so are Λ_1^{-1} and Λ_2^{-2}. Since $\Lambda = e^{i\kappa h}$, this reciprocity implies that if $\tilde{\kappa}$ is a solution, then so is $-\tilde{\kappa}$. Hence, the Bloch spectrum has axial spectral symmetry about $\kappa = 0$, i.e., $\omega(\kappa) = \omega(-\kappa)$, a symmetry that prohibits triple roots; this symmetry must be broken in order to obtain EP3. We note that Figotin and Vitebskiy (2003) provided a different proof of this necessary condition for the Bloch spectrum of layered dielectric media. Figotin and Vitebskiy (2003) further deduced that the Bloch diagram of wavevectors with only two components cannot form EP3 (see sections II.B and III.E therein). In the sequel, we show that the conclusion in elastodynamics is different: elastic waves in the $\left(x_1, x_2\right)$ plane may exhibit EP3. This difference is a manifestation of the coupling between the different in-plane elastic polarizations, which are absent in electrodynamics. This is evident in equation (83) in the paper of Figotin and Vitebskiy (2003), reflecting how the Bloch TE and TM modes decouple.

To this end, it is sufficient to include one layer that is made of anisotropic solid whose α_1 and α_2 coefficients are nonzero. In such case, the trace of its propagator matrix A is no longer zero, and hence the determinant of its transfer matrix—and the whole cell—is no longer 1. Specifically, $\det\mathsf{T} = e^{\mathrm{tr}\mathsf{A}^{(a)}h^{(a)}} = e^{-2ih^{(a)}k_2\alpha_2^{(a)}/\alpha_1^{(a)}}$, assuming material a is anisotropic. This breaks the reversibility property, and in turn the axial spectral symmetry, since I_4 and the coefficient of Λ^4 in Eq. (10) are no longer equal one to another. To the best of our knowledge, this is the first analysis for the condition of axial asymmetry in the Bloch spectrum of elastic laminates.

We conclude this part highlighting that the breakdown of axial symmetry does not violate the principle of reciprocity, which requires the frequency to be an even function of the wavevector, not the wavenumber, i.e., $\omega\left(\kappa, k_2\right) = \omega\left(-\kappa, -k_2\right)$, not $\omega\left(\kappa, k_2\right) = \omega\left(-\kappa, k_2\right)$.

[1] To see this, divide $p(\Lambda)$ by Λ^4 and observe that the result is $p\left(\Lambda^{-1}\right)$.

3.3. Consequences of reciprocity and energy conservation

When all the reciprocal constituents are conservative and $k_2 \in \mathbb{R}$, then T is J-unitary [see the paper by Langley (1996) and the references therein], i.e., it satisfies

$$\mathsf{T}^{\dagger}\mathsf{J}\mathsf{T} = \mathsf{J},\ \mathsf{J} = \begin{pmatrix} 0_2 & \mathrm{I}_2 \\ -\mathrm{I}_2 & 0_2 \end{pmatrix}, \tag{19}$$

where $\dagger$ is the conjugate-transpose operator. Indeed,

$$\mathsf{T}^{\dagger}\mathsf{J}\mathsf{T} = e^{\mathsf{A}^{\dagger}h}\mathsf{J}\mathsf{T} = e^{\mathsf{J}\mathsf{A}\mathsf{J}^{-\mathrm{T}}h}\mathsf{J}\mathsf{T} = \mathsf{J}\mathsf{T}^{-1}\mathsf{J}^{-1}\mathsf{J}\mathsf{T} = \mathsf{J}, \tag{20}$$

where we have used fact that A satisfies $(\mathsf{J}\mathsf{A})^{\dagger} = \mathsf{J}\mathsf{A}$, together with the identities $\mathsf{J}^{\mathrm{T}} = -\mathsf{J}$ and $e^{-\mathsf{J}\mathsf{A}\mathsf{J}^{-1}h} = \mathsf{J}e^{-\mathsf{A}h}\mathsf{J}^{-1}$. Since T is J-unitary, both Λ and $1/\Lambda^{*}$ satisfy Eq. (10), and hence so are both κ and κ^{*}. To show this, operate $\dagger$ on the eigenvalue problem of the inverse transfer matrix $\mathsf{T}^{-1}\mathsf{s} = \Lambda^{-1}\mathsf{s}$ and multiply by J to obtain

$$\mathsf{s}^{\dagger}\mathsf{T}^{-\dagger}\mathsf{J} = \left(\Lambda^{-1}\right)^{*}\mathsf{s}^{\dagger}\mathsf{J}. \tag{21}$$

Using the J-unitarity (19) and the identity $\mathsf{J}^{\mathrm{T}} = -\mathsf{J}$ we obtain

$$\left(\mathsf{J}\mathsf{s}^{*}\right)^{\mathrm{T}}\mathsf{T} = \left(\Lambda^{-1}\right)^{*}\left(\mathsf{J}\mathsf{s}^{*}\right)^{\mathrm{T}}, \tag{22}$$

i.e., $\left(\Lambda^{-1}\right)^{*}$ is also an eigenvalue of T, the eigenvector of which is $(\mathsf{J}\mathsf{s}^{*})^{\mathrm{T}}$.

3.4. Energy flux

The concept of energy flux in periodic media made of anisotropic materials may be foreign. For the convenience of the reader, we record some essential notions in Appendix B, and utilize their implications to our problem. We begin with the conclusion that the spatio-temporal mean energy flux in the axial direction is (Willis, 2015)

$$\langle \mathcal{P}_1 \rangle := -\frac{1}{2}\mathrm{Re}\left\langle \sigma_{1j}\dot{u}_j^{*}\right\rangle = \frac{\partial\omega}{\partial\kappa}\langle E\rangle, \tag{23}$$

where angular brackets denote spatial mean over the unit cell, $\mathcal{P}_1$ is the time-average energy flow in the x_1-direction, and

$$E = \frac{1}{4}\sigma_{ij}u_{i,j}^{*} + \frac{1}{4}\omega^2\rho u_k^{*}u_k \equiv \frac{1}{2}\omega^2\rho u_k^{*}u_k \tag{24}$$

is the time-average total energy density. It follows that the mean axial energy flux vanishes when the axial group velocity, i.e., the slope of the dispersion curve $\partial_\kappa\omega$ is zero, *if* $\langle E\rangle$ *is bounded*. This is the case at EP2, there $\langle E\rangle$ is finite and $\partial_\kappa\omega = 0$. As we demonstrate in the sequel, the total energy density abnormally diverges near EP3, at the same rate that $\partial_\kappa\omega$ tends to vanish. Specifically, Eq. (13) implies that near EP3

$$\frac{\partial\omega}{\partial\kappa} \propto \left(\kappa - \kappa_{\mathrm{EP3}}\right)^2 \propto \left(\omega - \omega_{\mathrm{EP3}}\right)^{2/3}, \tag{25}$$

and hence the mean energy density scales as $(\omega - \omega_{\mathrm{EP3}})^{-2/3}$, such that the energy flux is of order 1 (Figotin and Vitebskiy, 2006).

Some key properties of $\mathcal{P}_1$ are easy to demonstrate once it is recast in terms of s as

$$\mathcal{P}_1 = -\frac{1}{4}\omega\mathsf{s}^{*\mathrm{T}}\mathsf{J}\mathsf{s} =: [\mathsf{s},\mathsf{s}]. \tag{26}$$

Note that for any arbitrary $\mathsf{s}^{(m)}$ and $\mathsf{s}^{(n)}$

$$\left[\mathsf{T}\mathsf{s}^{(m)},\mathsf{T}\mathsf{s}^{(n)}\right] = \left[\mathsf{s}^{(m)},\mathsf{s}^{(n)}\right], \tag{27}$$

since T is J-unitary. If $\mathsf{s}^{(m)}$ and $\mathsf{s}^{(n)}$ are eigenvectors of T with eigenvalues $\Lambda^{(n)}$ and $\Lambda^{(m)}$, then together with Eq. (27), it follows that

$$\left[\mathsf{T}\mathsf{s}^{(m)},\mathsf{T}\mathsf{s}^{(n)}\right] = \left[\Lambda^{(m)}\mathsf{s}^{(m)},\Lambda^{(n)}\mathsf{s}^{(n)}\right] = \left[\mathsf{s}^{(m)},\mathsf{s}^{(n)}\right]. \tag{28}$$

Therefore, if $\Lambda^{*(m)}\Lambda^{(n)} \neq 1$, i.e., if $\kappa^{*(m)} \neq \kappa^{(n)}$, then $\left[\mathsf{s}^{(m)},\mathsf{s}^{(n)}\right] = 0$. This implies the important conclusion that a single propagating state vector with real κ carries energy in the axial direction, while a single evanescent state vector whose κ is complex or imaginary cannot carry energy along x_1. However, if the total state vector is composed of a sum of evanescent state vectors with conjugate wavenumbers, then their interaction carries energy along x_1. In semi-infinite laminates, such a scenario is excluded because one of the evanescent waves diverges at infinity, making it non-physical, while decaying evanescent modes that do not transport energy form to accommodate continuity conditions at interface problems (Srivastava and Willis, 2017). These observations allow us to restrict the interpretation of $\partial_\kappa\omega$ to real κ. In the sequel, we refer to modes with real κ as propagating modes.

Finally, we observe that $\mathcal{P}_1$ is independent of x_1, and hence $\langle\mathcal{P}_1\rangle = \mathcal{P}_1$. The conservation of $\mathcal{P}_1$ along x_1 results from the continuity of s in that direction. (See analogue proof for the antiplane shear problem by Srivastava and Willis, 2017, section 5c.)

We note that Eqs. (26)–(28) are essentially adaptation of the results that appear in section 5.5 of the paper by Figotin and Vitebskiy (2006), to our formulation for elastic laminates.

Table 1
Properties of two exemplary materials used as the constituents in Fig. 2.

Material	C_{11} [GPa]	C_{22} [GPa]	C_{66} [GPa]	C_{12} [GPa]	C_{16} [GPa]	C_{26} [GPa]	ρ [Kg/m^3]
a	276	276	78.8	118	50	0	7800
b	7.28	7.28	1.21	4.86	0	0	1200

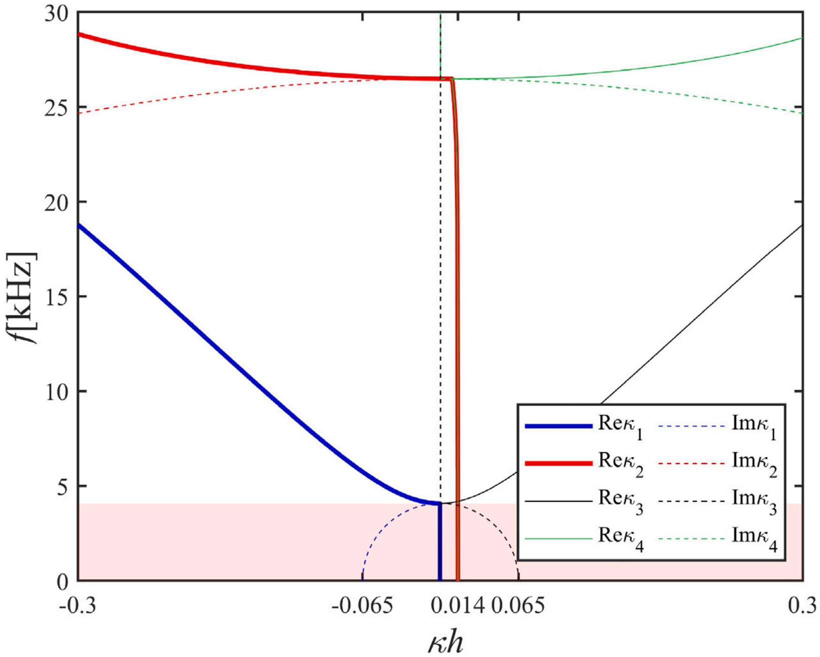

Fig. 2. Bloch spectrum of the exemplary laminate, whose constituents properties are given in Table 1, for $k_2h = 0.15$. Real (imaginary) part of each Bloch wavenumber is shown in solid (dashed) curve. Red shading denotes frequency band gap, without any propagating modes. The axial spectral symmetry of the diagram with respect to $\kappa = 0$ is broken.

4. Parametric spectra and implications on elastic wave scattering

This Section provides parametric examples of the our analytical analysis. First, it exemplifies that indeed the spectral axial symmetry of periodic laminates may be broken using anisotropic materials. Then, it shows that our design rules tune such spectra to exhibit EP3. Finally, it revisits the canonical interface problem between a homogeneous half-space and a semi-infinite laminate (Joseph and Craster, 2015; Lustig et al., 2019), and demonstrates that our design parameters lead to axially frozen modes in the laminate.

4.1. Bloch spectra

We begin by exemplifying the breakdown of axial symmetry by periodizing one isotropic material of thickness 3 mm and one anisotropic material of thickness 1.3 mm, whose properties are given in Table 1.

Fig. 2 presents the Bloch spectrum of the resultant infinite laminate in terms of the ordinary frequency $f = \omega/2\pi$, for $k_2h = 0.15$, where the real (imaginary) part of each Bloch wavenumber is shown in solid (dashed) curve. In accordance with our arguments in Section 3, the axial spectral symmetry of the diagram with respect to $\kappa = 0$ is broken. For example, at $f = 0\,\text{kHz}$, the red and green branches are complex conjugates, whose values are $0.014 \pm 0.9i$ (the imaginary part is outside the displayed region of κh values), while there are no branches with the values $-0.014 \pm 0.9i$ (the remaining two branches are $\pm 0.065i$). There is EP2 at $f = 26.48\,\text{kHz}$, where the imaginary part of these branches vanishes and their identical real part splits according to a square root law. At $f = 28\,\text{kHz}$, the values of the green and red branches are 0.259 and −0.246, respectively, and the two remaining branches are 0.56 and −0.54 (again, outside the displayed region).

Having exemplified the broken axial symmetry by a laminate with anisotropic constituents, we proceed to tune the invariants via rationally chosen material properties and frequency, in order to satisfy Eqs. (15)–(16) and form EP3. Formally, we aim to minimize the objective function $\phi = |\Delta_0| + |\Delta_1|$ over the design space. We choose C_{16} and C_{22} of material a as the design parameters, since C_{16} changes all the invariants, while C_{22} changes all the invariants except I_4.

By application of the above scheme to the base materials in Table 1, we find that ϕ vanishes for $C_{16} = 61.25$ GPa, $C_{22} = 63.33\,\text{GPa}$ and $f \approx 4.15\,\text{kHz}$ (the remaining parameters are fixed at the values of the previous example). The resultant Bloch spectrum is shown

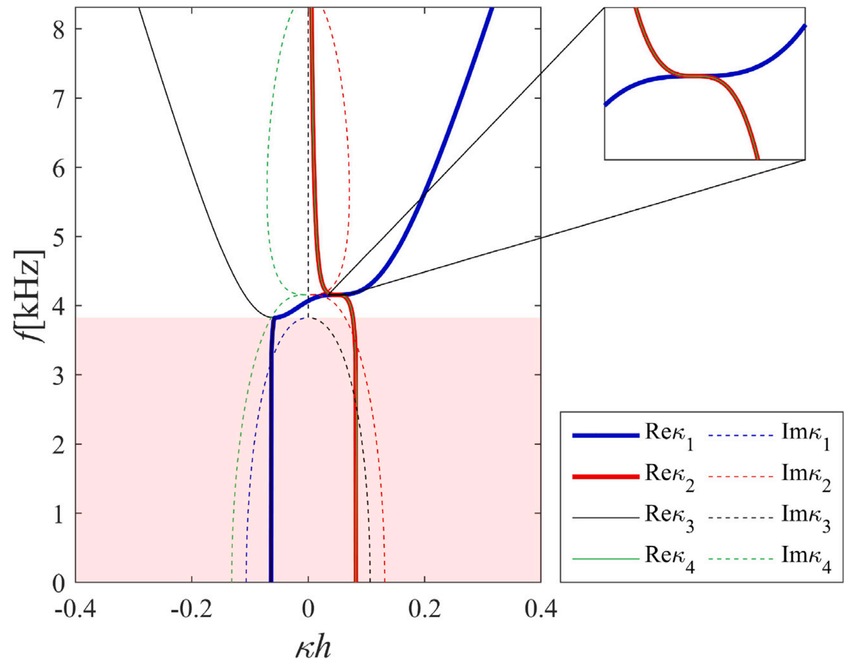

Fig. 3. Bloch spectrum of exemplary laminate, whose constituents properties satisfy the conditions for EP3, for $k_2 h = 0.15$. Real (imaginary) part of each Bloch wavenumber is shown in solid (dashed) curve. Red shading denotes frequency band gap, i.e., without any propagating modes. EP3 exists at $f \approx 4.15$ kHz, were the red, blue and green branches coalesce.

in Fig. 3. Indeed, the red, blue and green branches coalesce at $f_{\text{EP3}} \approx 4.15$ kHz to the value 0.048, (the value of the remaining black branch is -0.11), and follow cubic behavior close to the EP3. This is the first report of EP3 in the Bloch spectrum of planar elastic laminates.

4.2. The canonical scattering problem

We proceed to demonstrate the implications of the non-resonant Bloch EP3 on elastic wave propagation using a canonical scattering problem of a plane wave incident on a semi-infinite laminate (Joseph and Craster, 2015; Lustig et al., 2019). Specifically, we will show that the elastic transmittance of the laminate at EP3 is nonzero and can be even unity, in spite of the fact that the group velocity vanishes there.

To fix ideas, we consider a truncation of the designated laminate at $x_1 = 0$, there it is bonded to a homogeneous material occupying the half-space $x_1 < 0$. The question is to determine the reflected and transmitted waves from an incident wave propagating at an angle θ_i and amplitude I towards the interface (Fig. 1(b)). Standard analysis implies that the incident wave is partially reflected as pressure and shear waves of amplitudes R_L and R_S, respectively, and partially transmitted as a combination of two *forward* Bloch modes,[2] each of which can either be propagating with positive group velocity, or decaying with $\operatorname{Re}\kappa > 0$. The solution process selects the proper transmitted modes from the Bloch spectrum, and determines the amplitude of each scattered mode from the continuity conditions at the interface, which at the outset enforce that all waves share the same vertical wavenumber, k_2. In terms of these modes, the continuity conditions about $x_1 = 0$ are

$$T_1 \mathrm{s}_1\left(0^+\right) + T_2 \mathrm{s}_2\left(0^+\right) = I \mathrm{s}_I\left(0^-\right) + R_L \mathrm{s}_L\left(0^-\right) + R_S \mathrm{s}_S\left(0^-\right), \tag{29}$$

where T_1 and T_2 are the amplitude of the two transmitted Bloch modes s_1 and s_2, and s_L (s_S) is the reflected pressure (shear) mode. Eq. (29) constitutes four algebraic equations for the four amplitudes R_L, R_S, T_1 and T_2. As a consistency check for our solution, we verify that it respects energy conservation at the interface, such that the reflected and transmitted energy through the interface equals the incoming energy. The energy conservation equation in the axial direction takes the form

$$\frac{1}{|I|^2 \mathcal{P}_1^I}\left[\Sigma_{i=1}^2 \left|T_i\right|^2 \mathcal{P}_1^{T_i} - \left|R_L\right|^2 \mathcal{P}_1^{R_L} - \left|R_S\right|^2 \; \mathcal{P}_1^{R_S}\right] = 1, \tag{30}$$

[2] This construction holds almost always, i.e., except at discrete EP frequencies, there a more complicated construction is needed. We exploit the fact that we can use this construction arbitrarily close to EPs, for simplicity.

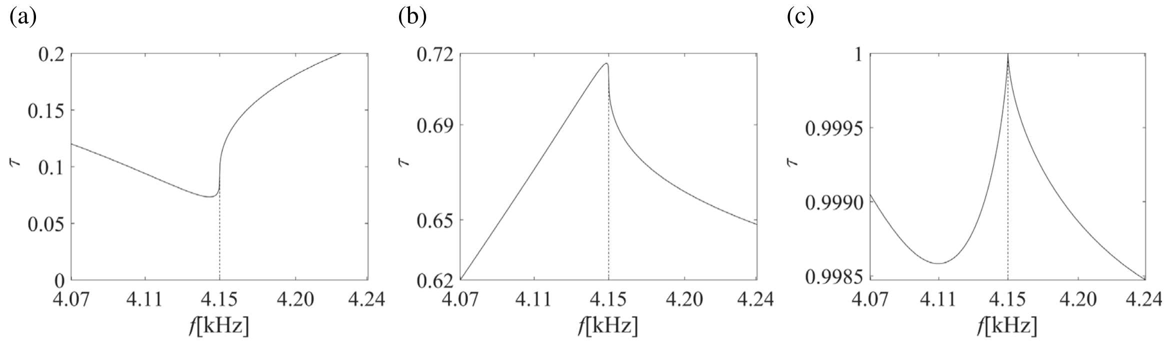

Fig. 4. Transmittance versus frequency of the laminate from Fig. 3, when incident (a) pressure; and (b) shear waves are incoming from half-space (32) at $k_2h = 0.15$. The dashed line denotes f_{EP3}. The transmittance is finite at f_{EP3}, even though there the group velocity vanishes. (c) Same as (b), only now shear waves are incoming from half-space (33). Strikingly, the transmittance is unity at f_{EP3}, there it forms a cusp.

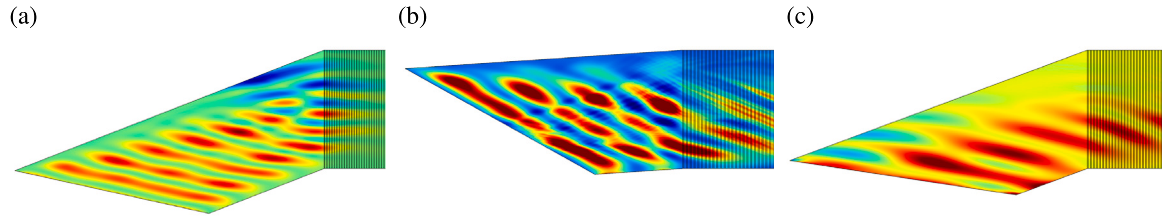

Fig. 5. Finite element simulations corresponding to Fig. 4 using the commercial code COMSOL showing energy flux along x_1 direction at EP3, when incident (a) pressure; and (b) shear waves are incoming from half-space (32) at $k_2h = 0.15$. (c) Same as (b), only now shear waves are incoming from half-space (33).

where $\mathcal{P}_1^{T_i} = \left[\mathrm{s}_{T_i}, \mathrm{s}_{T_i}\right]$ and so on. Note that the total transmitted energy flux is the sum of the energy flux of the two Bloch waves, in light of the results in Section 3.4. Also note that Eq. (30) can also be deduced from the continuity conditions (29). The scheme described above provides exact solution to the canonical scattering problem.

4.3. Transmittance near third-exceptional points

The transmittance of the semi-infinite laminate is defined by the ratio of the axial transmitted energy flux to the incident energy. Accordingly, the transmittance in our case is

$$\tau = \frac{\Sigma_{i=1}^{2} \left|T_i\right|^2 \mathcal{P}_1^{T_i}}{|I|^2 \mathcal{P}_1^{I}}. \tag{31}$$

Having at hand the exact solution to the scattering problem, we proceed to evaluate the transmittance using specific parameters in the frequency range that contains the EP3.

In our first parametric demonstration, we consider a half-space whose mechanical properties were arbitrarily set to

$$\mu^{(0)} = 0.178\,\mathrm{GPa},\, \lambda^{(0)} = 0.714\,\mathrm{GPa},\, \rho^{(0)} = 3000\,\mathrm{kg/m^3}. \tag{32}$$

The half-space guides waves at frequencies and angles whose resultant vertical wavenumber is $k_2h = k\cos\theta_i\, h = 0.15$,[3] so that Fig. 3 can be used to determine the transmitted modes.

Fig. 4(a) shows the transmittance extracted from our exact solution as function of frequency for incident pressure waves; the EP3 frequency is denoted by the dashed line. Indeed, the transmittance at the EP3 is nonzero, in spite of the fact that the respective group velocity is zero. The particular transmittance value depends on the incident wave properties, and in particular its polarization. This is evident in Fig. 4(b), which is the same as Fig. 4(a), only for incident shear waves. We observe that the transmittance peaks near the EP3 to $\tau \approx 0.71$, which is significantly higher than the transmittance in Fig. 4(a).

It is possible to achieve unity transmittance by tailoring the incoming wave, or equivalently, the properties of the waveguide, i.e., the homogeneous half-space. Indeed, by optimizing over $\lambda^{(0)}$, $\mu^{(0)}$ and $\rho^{(0)}$ we find that the set

$$\mu^{(0)} = 1.11\,\mathrm{GPa},\, \lambda^{(0)} = 2.01\,\mathrm{GPa},\, \rho^{(0)} = 2800\,\mathrm{kg/m^3}, \tag{33}$$

[3] The pressure (shear) wave velocity in the half-space is $c_L^{(0)} = \sqrt{\left(2\mu^{(0)} + \lambda^{(0)}\right)/\rho^{(0)}}$ ($c_S^{(0)} = \sqrt{\mu^{(0)}/\rho^{(0)}}$) and the wavenumber is $k = \omega/c_L^{(0)}$ ($k = \omega/c_S^{(0)}$).

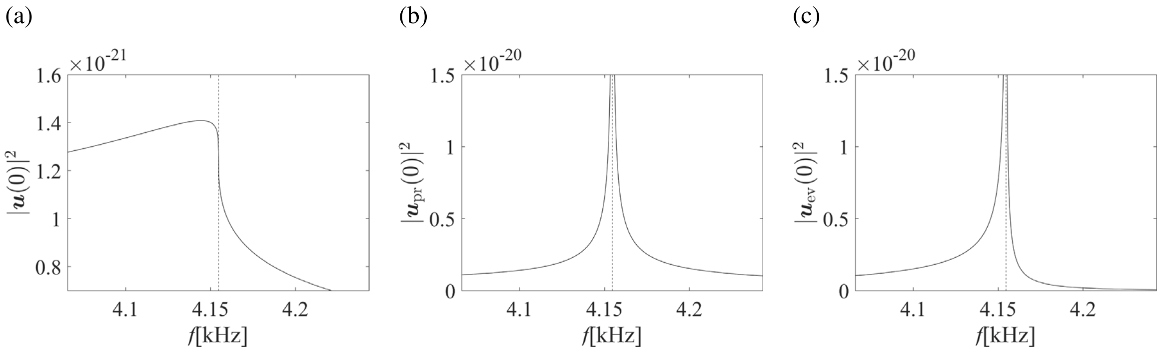

Fig. 6. Squared magnitude of the (a) total; (b) propagating; and (c) evanescent displacement fields at $x_1 = 0$, as functions of frequency, when shear waves are incoming from half-space (33) at $k_2 h = 0.15$. The propagating- and evanescent displacement fields diverge when $f \to f_{\rm EP3}$ (denoted by a dashed line), while $\boldsymbol{u}(0) = \boldsymbol{u}_{\rm pr}(0) + \boldsymbol{u}_{\rm ev}(0)$ remains finite, as it should to satisfy interface continuity conditions.

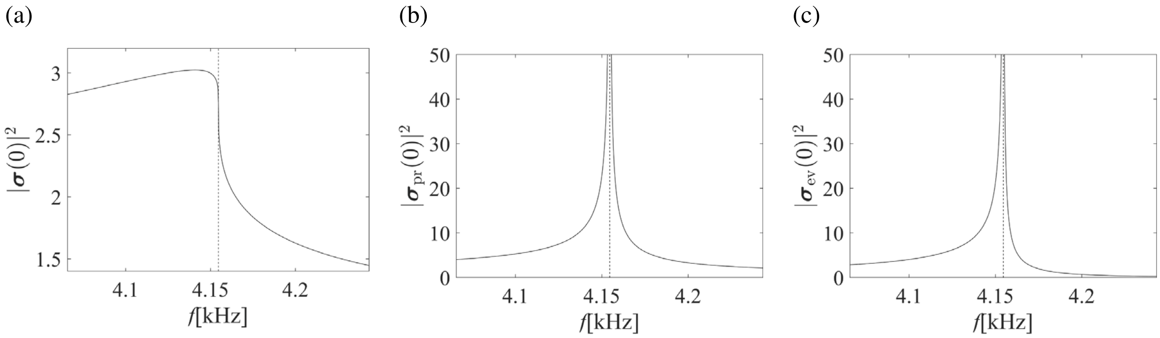

Fig. 7. Squared magnitude of the (a) total; (b) propagating; and (c) evanescent stress fields at $x_1 = 0$, as functions of frequency, when shear waves are incoming from half-space (33) at $k_2 h = 0.15$. The propagating- and evanescent stress fields diverge when $f \to f_{\rm EP3}$ (denoted by a dashed line), while $\boldsymbol{\sigma}(0) = \boldsymbol{\sigma}_{\rm pr}(0) + \boldsymbol{\sigma}_{\rm ev}(0)$ remains finite, as it should to satisfy interface continuity conditions.

generates unity transmittance at the EP3. We demonstrate this in Fig. 4(c), which shows $\tau(f)$ of shear waves incoming from the optimized waveguide. Indeed, the transmittance reaches unity at the EP3, there it forms a cusp.

To support the results that are based on the exact solution, we also carry out full-field finite element simulations using the commercial code COMSOL. In these simulations, we generate plane wave packets at $f = 4.15$ kHz and different incident angles using a line load in a homogeneous medium, and calculate the fields that are transmitted through the laminate (see Appendix C for a detailed description of the computational model).

Fig. 5 shows exemplary time snapshots of the energy flux along x_1, extracted from COMSOL's models that simulate the cases in Fig. 4. Fig. 5(a) corresponds to pressure waves incident from material (32) at an angle $\theta_i = 36.97°$. The simulation yielded a transmittance of 0.086 and refraction angle $\theta_{\rm tr} = 2.87°$ ($\tan\theta_{\rm tr} := \langle \mathcal{P}_1^T \rangle / \langle \mathcal{P}_2^T \rangle$) where our analytical calculation yielded $\tau = 0.0735$ and $\theta_{\rm tr} = 2.42°$.

Fig. 5(b) corresponds to shear waves incident from material (32) at an angle $\theta_i = 70.98°$. The transmittance and refraction angle from the simulation are 0.6 and 17.93°, respectively, where the analytical predictions are $\tau = 0.71$ and 15.25°, respectively. Thus, both the analytical calculation and computational simulation predict a substantial amount of transmitted energy near the EP3, when the polarization of the incident wave is transverse. Lastly, Fig. 5(c) corresponds to shear waves that are incoming from the optimized material (33) at angle 32.61°. The transmittance in the simulation is 0.9, which is less than 10% error w.r.t. the analytical prediction of 0.99. The refraction angle in the simulation is 7.85°, less than one degree away from its analytical calculation of 6.87°.

4.4. Mode coalescence, evanescent boundary layer and saturation

The purpose of this part is to elucidate the physical origins of the anomalous transmission, by analyzing its comprising modes. At the outset, we recall that finite transmittance can concurrently occur with vanishing group velocity only if the energy density diverges. To show that this is indeed the case, we evaluate the transmitted fields at frequencies in the vicinity of the EP3, recalling that the total energy density is a quadratic function of the displacement field.

Specifically, Figs. 6(a), 6(b) and 6(c) show the squared magnitude of the total-, propagating- and evanescent displacement field, respectively, versus the frequency, evaluated at the interface, when shear waves are incoming from half-space (33). The propagating displacement field diverges when the frequency approaches the EP3 frequency, and hence so does its energy density. The evanescent

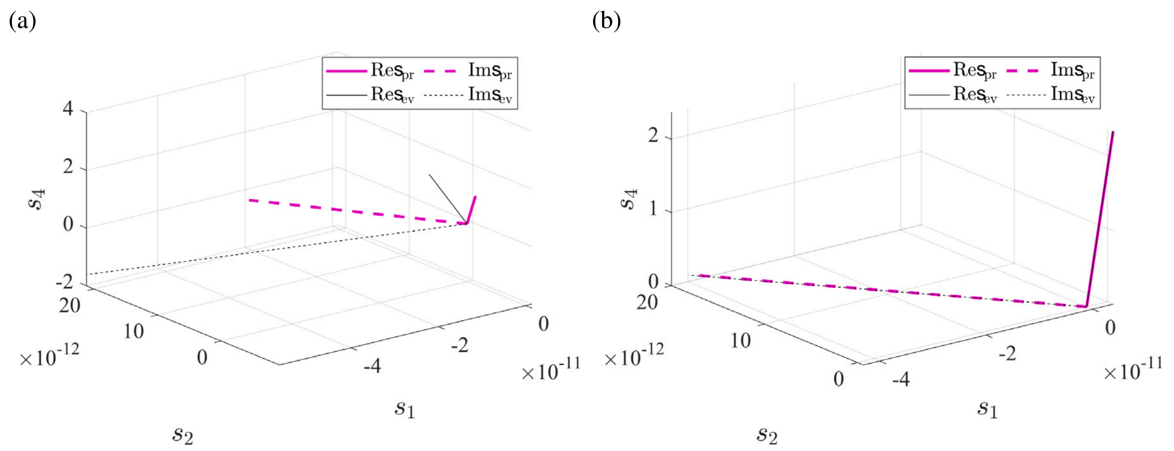

Fig. 8. Projection of the two normalized forward state vectors onto the (s_1, s_2, s_4)-space, at (a) $f = 4.2$ kHz; and (b) 4.155 kHz. Real (imaginary) part of s_{ev} (s_{pr}) is denoted in black (purple). The state vectors tend to align, as the frequency approaches f_{EP3}.

displacement field diverges as well, while the total displacement field, which is the sum of $\mathbf{u}_{\mathrm{pr}}$ and $\mathbf{u}_{\mathrm{ev}}$, remains finite as it should to satisfy continuity conditions at the interface.

Fig. 7 mirrors Fig. 6 for the stress fields, which exhibit the same trends as the displacement fields. We note that all of the displacement- and stress components, i.e., u_1, u_2, σ_{21} and σ_{22}, diverge, although we do not present that, for brevity. These components diverge in a way that the state vectors of the propagating- and evanescent modes become collinear as $f \to f_{\mathrm{EP3}}$. This tendency is the hallmark of exceptional points of non-Hermitian systems, at which both the eigenvalues and the eigenvectors become degenerate.

To show this, we present in Fig. 8 the two forward state vectors at two frequencies, namely, at $f = 4.2$ kHz (Fig. 8(a)) and $f = 4.155$ kHz (Fig. 8(b)). Specifically, we normalize the vectors such that $s_3 = |1|$, and depict their projection on the three-dimensional space (s_1, s_2, s_4), to facilitate visualization. The real (imaginary) part of s_{ev} (s_{pr}) is denoted in black (purple). Indeed, we observe how the state vectors tend to align as the frequency approaches f_{EP3}.

Another manifestation of this alignment is illustrated in Fig. 9, which shows the distribution of the vertical displacement over the unit cell of the two forward modes at $f = 4.2$ kHz (panel a); and 4.155 kHz (panel b). Real (imaginary) part of u_2^{ev} (u_2^{pr}) is denoted in black (purple). We observe how the eigenfunctions tend to align as the frequency approaches f_{EP3}. Panels (c) and (d) mirror panels (a) and (b), only for the normal stress σ_{11}, showing a similar trend.

Collectively, Figs. 6–8 demonstrate how

$$\mathrm{s}_{\mathrm{pr}}(0) \approx -\mathrm{s}_{\mathrm{ev}}(0) \propto |f - f_{\mathrm{EP3}}|^{-1/3}, \tag{34}$$

as $f \to f_{\mathrm{EP3}}$; the total field resulting from this destructive interference is sufficiently small to accommodate the continuity conditions (29) at the interface between the half-space and the laminate.

We recall that the Bloch theorem (7) implies that the evanescent mode spatially decays at the rate $e^{-x_1 \mathrm{Im}\kappa}$. By contrast, real κ in Eq. (7) yields constant amplitude of the propagating mode. Hence, the evanescent mode creates a boundary layer near $x_1 = 0$, beyond which its contribution is negligible relative to the propagating mode. We follow Srivastava and Willis (2017), who defined the end of the boundary layer at the distance where the magnitude of the evanescent mode is 10% of its amplitude at the interface. Since $(\mathrm{Im}\,\kappa)^{-1} \propto |f - f_{\mathrm{EP3}}|^{-1/3}$, the boundary layer elongates as $f \to f_{\mathrm{EP3}}$. We demonstrate this phenomenon in Figs. 10(a), 10(b) and 10(c), which respectively show the squared magnitude of the total-, propagating- and evanescent displacement field as functions of the distance from the interface. Indeed, we observe how the propagating mode maintains a constant magnitude, while the evanescent mode undergoes exponential decay. As a result, the total displacement converges to propagating mode beyond the evanescent boundary layer. In view of Eq. (34), this saturation value is two order of magnitudes greater than the magnitude of the incident wave. We note that the rest of the field variables follow a similar trend, hence are not shown for brevity.

To further highlight these aspects of spatial evolution of the transmitted fields, we present in Fig. 11(a) the real part of u_1, u_1^{ev} and u_1^{pr} along the first 5 unit cells near the interface. In agreement with Eq. (34), the propagating (pink curve) and evanescent (thin black) components are opposite in sign and their sum, i.e., Reu_1 (thick blue), is two order of magnitudes smaller, namely,

$$\mathrm{Re}\,u_1^{\mathrm{ev}}, \mathrm{Re}\,u_1^{\mathrm{pr}} \gg \mathrm{Re}\,u_1^{\mathrm{ev}} + \mathrm{Re}\,u_1^{\mathrm{pr}} = \mathrm{Re}\,u_1. \tag{35}$$

We reiterate that this destructive interference follows Eq. (34) in a way that satisfies the continuity conditions [Eq. (29)] at the interface ($x_1 = 0$).

The propagating and evanescent modes fluctuate within their respective envelopes (Figs. 10(b) and 10(c), respectively). Fig. 11(b) depicts these fluctuations across two additional segments of length $5h$: one segment that originates at $x_1 = 6500h$ (curves with diamond marks) and is inside the boundary layer; and a second segment that originates at $x_1 = 30000h$ and is beyond the boundary layer (solid curves). We observe how the evanescent mode decays and its value about $x_1 = 30000h$ is at the order 10^{-10}, such that the axial displacement is approximately equal to the propagating mode, which maintains its amplitude. The imaginary part of the axial displacement exhibits similar features up to a phase shift, hence omitted for brevity.

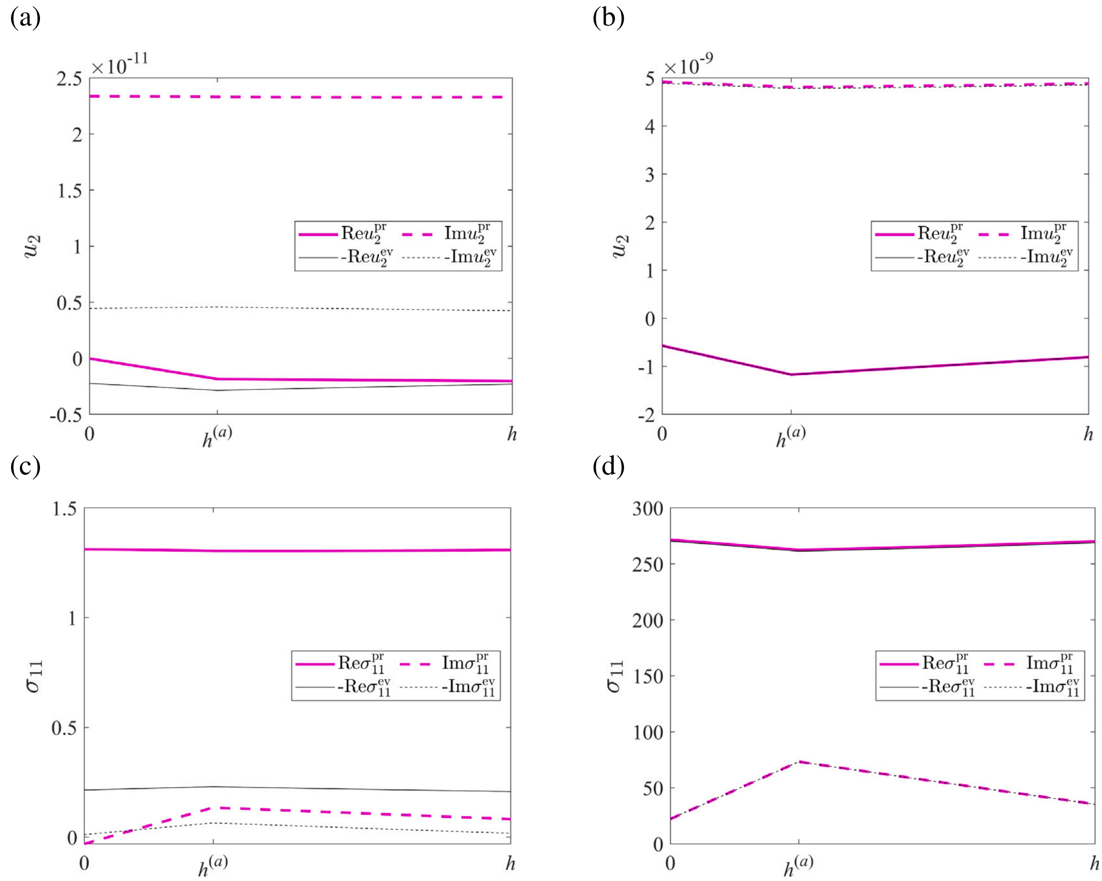

Fig. 9. Vertical displacement distribution over the unit cell of the two forward modes at (a) $f = 4.2\,\mathrm{kHz}$; and (b) $4.155\,\mathrm{kHz}$. Real (imaginary) part of u_2^{ev} (u_2^{pr}) is denoted in black (purple). Panels (c) and (d) are the same as (a) and (b), only for the normal stress σ_{11}. Collectively, they demonstrate how the eigenfunctions tend to align as the frequency approaches f_{EP3}.

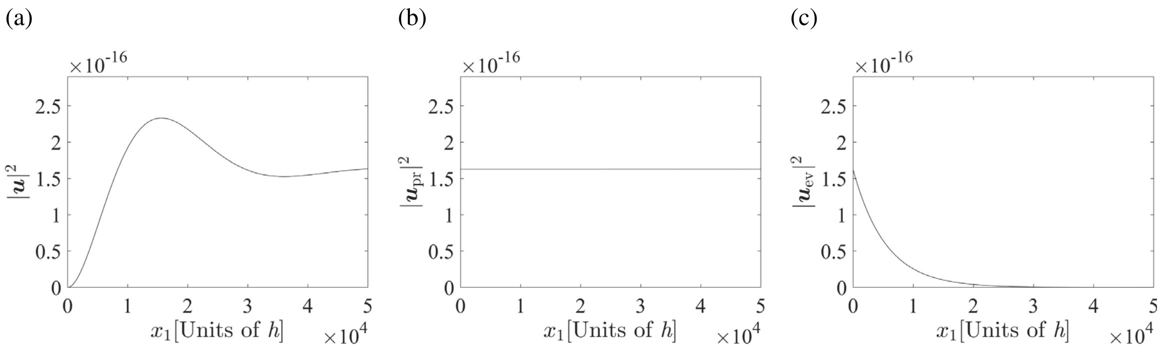

Fig. 10. Squared magnitude of the (a) total; (b) propagating; and (c) evanescent displacement fields as functions of the distance from the interface. The magnitude of $\boldsymbol{u}_{\mathrm{pr}}$ remains constant, while that of $\boldsymbol{u}_{\mathrm{ev}}$ vanishes, and hence $|\boldsymbol{u}|^2 \to |\boldsymbol{u}_{\mathrm{pr}}|^2$ away from the interface.

5. Conclusions

We derived the conditions for the coalescence of three natural modes in the spectrum of periodic elastic laminates composed of two materials. This non-resonant exceptional point (EP) occurs in the Bloch spectrum, distinct from resonant EPs which are the focus of most works. The first report of this type of non-resonant, third-order EP (EP3) was by Figotin and Vitebskiy (2003) for electromagnetic waves; one of their conclusions was that in order to form EP3, the wavevector must have inclination in both the horizontal and vertical directions. We showed that it is sufficient for elastic waves to have inclination only in the vertical

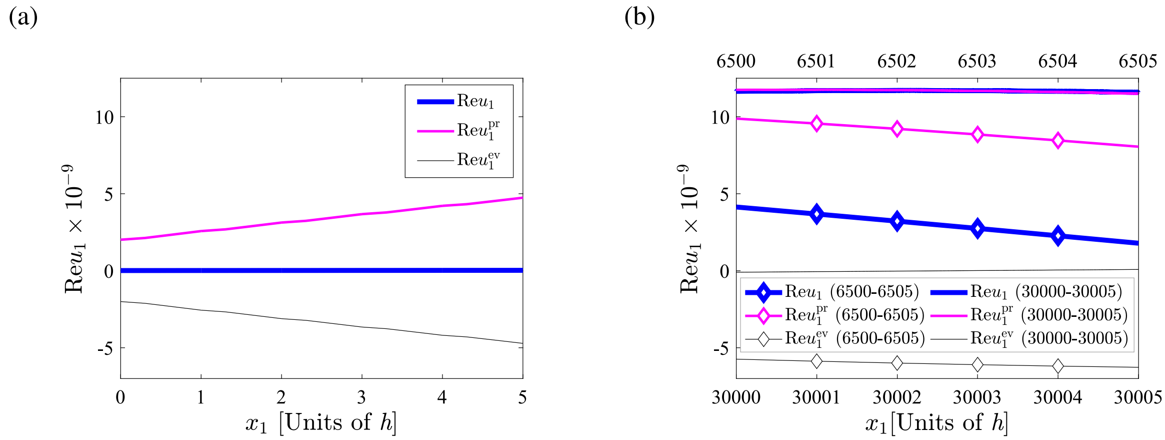

Fig. 11. The axial displacement across different segments of length $5h$. (a) Near the interface with the half-space. Thin black, purple and thick blue curves denote the real part of axial component of the evanescent boundary layer mode, propagating mode and total displacement, respectively. The individual modes are opposite in sign and their sum satisfies the continuity conditions. (b) Inside the boundary layer at $x_1 = 6500h$ (curves with diamond marks); and beyond the boundary layer at $30000h$ (solid curves). The evanescent mode decays and its value about $x_1 = 30000h$ is at the order 10^{-10}, such that the total axial displacement is approximately equal to the propagating mode, which maintains its amplitude.

direction, i.e., to consider planar settings, in order to exhibit EP3. This practical simplification results from the tensorial richness in elastodynamics, relative to electrodynamics.

Our analysis provides simple arguments for the need in axial spectral asymmetry to access EP3; and for the need in anisotropic constituents to break that spectral symmetry. These arguments and the resultant algebraic conditions for EP3 are simpler than those in the pioneering work of Figotin and Vitebskiy (2003). Our conclusions and derived conditions were never reported before, in spite of the fact that elastic waves propagation in stratified anisotropic materials is a classical problem (Nayfeh, 1995).

We have demonstrated the formation of EP3 using the parameters of exemplary anisotropic materials that satisfy our derived conditions. In electrodynamics, these EPs were shown to be associated with the generation of axially frozen modes in interface problems. Anomalously, the energy flux of these modes in the axial direction is finite, despite having zero group velocity in that direction (Figotin and Vitebskiy, 2003). In order to examine if it is possible to excite similar modes in planar elastic laminates, we have revisited the canonical scattering problem of a plane wave incident on a semi-infinite laminate. Our analysis showed that if the laminate is designed according to our criteria for EP3, then its total energy density diverges when the frequency approaches the EP3 frequency, at the same rate that the group velocity decays, such that the energy flux remains finite. We further showed that by shaping the incoming wave, it is possible to achieve unity transmittance at the EP3. To shed light on the physical origins of the axial frozen modes, we have analyzed their comprising modes. The analysis shows that the frozen modes are the sum of a propagating mode and an evanescent mode, which tend to align near the EP3; this coalescence is the hallmark of non-Hermitian degeneracies. Their amplitude at the interface diverges such that their sum is small enough to satisfy the continuity conditions at the interface. The evanescent mode decays away from the interface, forming a boundary layer beyond which the transmitted field converges to the propagating mode, which maintains a constant large amplitude.

CRediT authorship contribution statement

Ariel Fishman: Formal analysis, Investigation, Methodology, Validation, Writing – original draft. **Guy Elbaz:** Formal analysis, Methodology. **T. Venkatesh Varma:** Software, Validation. **Gal Shmuel:** Conceptualization, Formal analysis, Funding acquisition, Investigation, Methodology, Supervision, Visualization, Writing – original draft, Writing – review & editing.

Declaration of competing interest

The authors declare that they have no known competing financial interests or personal relationships that could have appeared to influence the work reported in this paper.

Data availability

No data was used for the research described in the article.

Acknowledgments

We thank anonymous reviewers for useful comments which helped us improve this paper. This project was funded by the European Union (ERC, EXCEPTIONAL, Project No. 101045494).

Appendix A. Derivation of Eq. (3)

Using Voigt notation for the components of $\mathbf{C}$, we can write the in-plane constitutive equations of anisotropic solids in the matrix form

$$\begin{pmatrix} \sigma_{11} \\ \sigma_{22} \\ \sigma_{21} \end{pmatrix} = \begin{pmatrix} C_{11} & C_{12} & C_{16} \\ C_{12} & C_{22} & C_{26} \\ C_{16} & C_{26} & C_{66} \end{pmatrix} \begin{pmatrix} \epsilon_{11} \\ \epsilon_{22} \\ 2\epsilon_{12} \end{pmatrix}, \tag{A.1}$$

where we recall that the components of the strain ϵ are related to the displacement field via $\epsilon = \left(\nabla \boldsymbol{u} + \nabla \boldsymbol{u}^{\mathrm{T}}\right)/2$. By inverting Eq. (A.1) and substituting the resultant expressions for substituting the expressions for ϵ_{11} and ϵ_{12} into the constitutive equation for σ_{22}, we have that

$$\sigma_{22} = \tfrac{1}{\alpha_1}[(\alpha_4 + C_{22}\alpha_1)u_{2,2} + \alpha_2\sigma_{12} + \alpha_3\sigma_{11}] \ , \tag{A.2}$$

where

$$\begin{aligned} \alpha_1 &= C_{16}^2 - C_{11}C_{66}, \qquad & \alpha_2 &= C_{12}C_{16} - C_{11}C_{26}, \\ \alpha_3 &= C_{16}C_{26} - C_{12}C_{66}, \qquad & \alpha_4 &= C_{12}^2 C_{66} - 2C_{12}C_{16}C_{26} + C_{11}C_{26}^2. \end{aligned} \tag{A.3}$$

Next, we rewrite the balance of linear momentum using (A.2) in the form

$$\begin{pmatrix} \sigma_{11} \\ \sigma_{21} \end{pmatrix}_{,1} = \frac{1}{\alpha_1} \begin{pmatrix} -\alpha_1\rho\omega^2 & 0 & 0 & -ik_2\alpha_1 \\ 0 & (\alpha_4 + C_{22}\alpha_1)k_2^2 - \alpha_1\rho\omega^2 & -ik_2\alpha_3 & -ik_2\alpha_2 \end{pmatrix} \begin{pmatrix} u_1 \\ u_2 \\ \sigma_{11} \\ \sigma_{21} \end{pmatrix}. \tag{A.4}$$

Combining Eq. (A.4) and the aforementioned relations for the strain components yields

$$\begin{pmatrix} u_1 \\ u_2 \\ \sigma_{11} \\ \sigma_{21} \end{pmatrix}_{,1} = \frac{1}{\alpha_1} \begin{pmatrix} 0 & -ik_2\alpha_3 & -C_{66} & C_{16} \\ -ik_2\alpha_1 & -ik_2\alpha_2 & C_{16} & -C_{11} \\ -\alpha_1\rho\omega^2 & 0 & 0 & -ik_2\alpha_1 \\ 0 & \alpha_4 k_2^2 - \alpha_1\alpha_5 & -ik_2\alpha_3 & -ik_2\alpha_2 \end{pmatrix} \begin{pmatrix} u_1 \\ u_2 \\ \sigma_{11} \\ \sigma_{21} \end{pmatrix}, \tag{A.5}$$

where $\alpha_5 = \rho\omega^2 - k_2^2 C_{22}$, or

$$\frac{\partial}{\partial x_1}\mathsf{s}\left(x_1\right) = \mathsf{A}\left(x_1\right)\mathsf{s}\left(x_1\right), \tag{A.6}$$

after factoring out the common x_2- and t dependencies.

Appendix B. On the energy flux in anisotropic solids and periodic media

The concepts detailed next can be found in the excellent treatises by Auld (1973) and Carcione (2001). We start with Poynting's theorem, leading to the notion of the acoustic Poynting vector

$$\boldsymbol{\mathcal{P}} := -\boldsymbol{\sigma}\cdot\dot{\mathbf{u}}, \tag{B.1}$$

which provides the power flow density. For time-harmonic fields described using complex variables, it is useful to define the complex Poynting vector as $-\boldsymbol{\sigma}\cdot\dot{\mathbf{u}}^*/2$, the real part of which is the time-average power flow density. With abuse of notation, we write

$$\boldsymbol{\mathcal{P}} = -\frac{1}{2}\mathrm{Re}\left(\boldsymbol{\sigma}\cdot\dot{\mathbf{u}}^*\right). \tag{B.2}$$

The reciprocity theorem leads to the important relation that the energy velocity $\boldsymbol{\mathcal{P}}/E$ equals to group velocity $\partial\omega/\partial\mathbf{k}$, or equivalently that

$$\boldsymbol{\mathcal{P}} = \frac{\partial\omega}{\partial\mathbf{k}}E, \tag{B.3}$$

where $\mathbf{k}$ is the wavevector, and we recall that E is the time-average total energy density [Eq. (24)]. So far, the treatment of homogeneous anisotropic media has been identical to that of isotropic media; it departs at the calculation of the group velocity. Homogeneous isotropic media are non-dispersive, such that $\boldsymbol{\mathcal{P}}$ and $\mathbf{k}$ parallel, and then the group velocity aligns with $\mathbf{k}$, and the phase velocity is direction-independent. By contrast, the solution of Christoffel equations reveals that anisotropic media are dispersive such that the phase velocity is direction-dependent. Accordingly, the group and energy velocities are not restricted to align with $\mathbf{k}$.

To get an intuitive sense for the group velocity, consider a pair of one-dimensional waves with the same amplitude but the frequency and wavenumber of the second wave are small variations of those of the first wave. As a result, the wave packet can be written as

$$\cos(kx - \omega t) + \cos[(k+\delta k)x - (\omega+\delta\omega)t] = 2\cos(\frac{1}{2}x\delta k - \frac{1}{2}t\delta\omega)\cos(\bar{k}x - \bar{\omega}t), \tag{B.4}$$

where $\bar{k}$ (resp. $\bar{\omega}$) is the average wavenumber (resp. frequency) of the two waves. Since $\delta k \ll \bar{k}$ and $\delta\omega \ll \bar{\omega}$, their function represents low frequency, long-wavelength modulation envelope of the high-frequency carrier, namely, $\cos(\bar{k}x - \bar{\omega}t)$. The velocity of

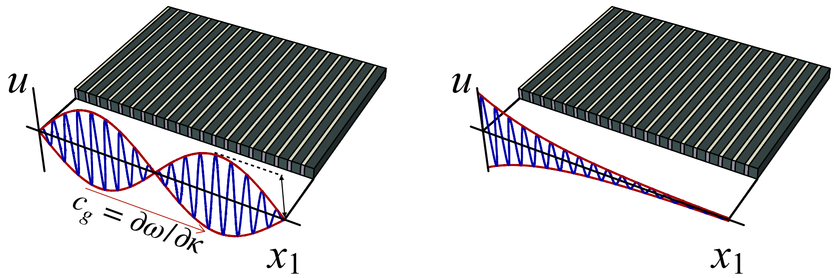

Fig. 12. (Left) Illustration of a wave packet in a 1D dispersive medium. The envelope of the packet (red curves) propagates in the axial direction with the group velocity $\partial_\kappa \omega$ at constant amplitude. Dispersion can originates either from material anisotropy or from geometrical periodicity, in which case κ is the real Bloch wavenumber. (Right) Illustration of evanescent Bloch wave with complex wavenumber, whose amplitude decays as function of x_1.

the modulation is $\delta\omega/\delta k$. By extending this idea to the superposition of infinite number of waves and to two-dimensional settings, we get that the velocity of the modulation envelope is $\partial\omega/\partial\mathbf{k}$, like the group velocity.

The energy flux in periodic media has much in common with the energy flux in anisotropic media. To point out the similarities between the two, we recall that the Bloch theorem states that free waves in periodic media must have the Bloch–Floquet form

$$\boldsymbol{u} = \tilde{\boldsymbol{u}}(\mathbf{x})\, e^{i(\boldsymbol{\kappa}\cdot\mathbf{x}-\omega t)},\ \boldsymbol{u}(\mathbf{x}+\mathbf{r}) = \boldsymbol{u}(\mathbf{x}), \tag{B.5}$$

where $\boldsymbol{\kappa}$ is the Bloch wavevector and $\mathbf{r}$ is any lattice vector which defines the periodicity of $\mathbf{C}$ and ρ. There are no assumptions on the symmetry of $\mathbf{C}$ in the derivation of the Bloch theorem, hence Eq. (B.5) holds for both isotropic and anisotropic periodic media. The Bloch wavevector and the frequency are related through the dispersion relation, hence periodic media are dispersive, like anisotropic homogeneous media. The concept of long-wavelength modulation envelope introduced for anisotropic homogeneous media is identified now with the Bloch envelope; and the group velocity is identified now with the velocity of that Bloch packet (see Fig. 12).

Analogous to Eq. (B.3), Willis (2015) has shown that for real Bloch wavevectors (see also Ref. Srivastava, 2016)

$$\langle \boldsymbol{\mathcal{P}} \rangle = \frac{\partial\omega}{\partial\boldsymbol{\kappa}} \langle E \rangle, \tag{B.6}$$

where the angle brackets $\langle\cdot\rangle$ denote averaging over one spatial period, i.e., over the unit cell. Like in the derivation of Eq. (B.3), no assumptions were made on the symmetry of $\mathbf{C}$ in the derivation of Eq. (B.6), except the usual ones that result from energy conservation and the symmetry of the strain and stress ($C_{ijkl} = C_{jikl} = C_{jilk} = C_{lkji}$), hence it holds at the level of generality of anisotropic constituents. Thus, like in homogeneous anisotropic media, the energy flux in periodic media made of isotropic constituents is not necessarily parallel to the wavevector. Furthermore, in both media there are also evanescent modes with complex wavenumber that do not carry energy on their own (see Section 3.4 and Fig. 12).

The similarities above between the energy flux in homogeneous anisotropic media and periodic media are not accidental: they are consistent with the fact that in the homogenization limit, periodic media made of isotropic materials effectively respond like homogeneous media with anisotropic effective properties (Laude et al., 2021). There are more than a few excellent works that show this, e.g., using Craster's irregular long-wavelength asymptotic dynamic homogenization (Antonakakis et al., 2014; Lefebvre et al., 2017).

In view of the above, the energy flux in the medium that we analyze, i.e., a laminate made of anisotropic phases, can be considered as the energy flux in a higher-rank laminate made of isotropic phases. The equations in Section 3.4 are specialization of some of the equations given here to the case where the periodicity is only along x_1.

Appendix C. Finite element computational simulations

For our computational simulations, we used the solid mechanics module with time-dependent study in the finite element-based commercial software COMSOL Multiphysics® 5.6. We excited 40 cycles of sinusoidal waves at a line load which is located at the left edge of the homogeneous material; to excite pressure (shear) waves, the excitation direction is normal (parallel) to the line load. To reduce spurious reflections at the spatial domain boundaries, we used COMSOL's low-reflecting boundary conditions. The domain is discretized into a four-node structured quadrilateral mesh with a maximum element size of 4 mm. The element size was chosen such that it is less than one-sixth of the wavelength of the wave under consideration. We set a relative tolerance of 0.1% in error for the convergence of the finite element analyses. To estimate the energy flux, and in turn the transmittance and refraction angles, we have calculated the line average of the mechanical energy flux.

References

Achilleos, V., Theocharis, G., Richoux, O., Pagneux, V., 2017. Non-Hermitian acoustic metamaterials: Role of exceptional points in sound absorption. Phys. Rev. B 95, 144303. http://dx.doi.org/10.1103/PhysRevB.95.144303, URL https://link.aps.org/doi/10.1103/PhysRevB.95.144303.

Adams, Samuel D.M., Craster, Richard V., Guenneau, Sebastien., 2009. Guided and standing bloch waves in periodic elastic strips. Waves Random Complex Media 19 (2), 321–346. http://dx.doi.org/10.1080/17455030802541566.

Antonakakis, T., Craster, R.V., Guenneau, S., 2014. Homogenisation for elastic photonic crystals and dynamic anisotropy. J. Mech. Phys. Solids (ISSN: 0022-5096) 71, 84–96. http://dx.doi.org/10.1016/j.jmps.2014.06.006, URL http://www.sciencedirect.com/science/article/pii/S0022509614001252.

Apaydin, N., Zhang, L., Sertel, K., Volakis, J.L., 2012. Experimental validation of frozen modes guided on printed coupled transmission lines. IEEE Trans. Microw. Theory Tech. 60 (6), 1513–1519. http://dx.doi.org/10.1109/TMTT.2012.2192746.

Ashida, Yuto, Gong, Zongping, Ueda, Masahito, 2020. Non-Hermitian physics. Adv. Phys. 69 (3), 249–435. http://dx.doi.org/10.1080/00018732.2021.1876991.

Assouar, Badreddine, Liang, Bin, Wu, Ying, Li, Yong, Cheng, Jian-Chun, Jing, Yun, 2018. Acoustic metasurfaces. Nat. Rev. Mater. 3 (12), 460–472. http://dx.doi.org/10.1038/s41578-018-0061-4.

Auld, B.A., 1973. Acoustic Fields and Waves in Solids. A Wiley-Interscience Publication, Wiley, ISBN: 9785885013437, URL https://books.google.co.il/books?id=_2MWAwAAQBAJ.

Benzaouia, Mohammed, Stone, A.D., Johnson, Steven G., 2022. Nonlinear exceptional-point lasing with ab initio Maxwell–Bloch theory. APL Photonics (ISSN: 2378-0967) 7 (12), 121303. http://dx.doi.org/10.1063/5.0105963.

Bigoni, D., Kirillov, O. (Eds.), 2019. Dynamic Stability and Bifurcation in Nonconservative Mechanics, vol. 586, pp. 1–190. http://dx.doi.org/10.1007/978-3-319-93722-9, ISBN 0254-1971; 2309-3706; 978-3-319-93722-9; 978-3-319-93721-2.

Braga, Arthur M.B., Herrmann, George, 1992. Floquet waves in anisotropic periodically layered composites. J. Acoust. Soc. Am. (ISSN: 0001-4966) 91 (3), 1211–1227. http://dx.doi.org/10.1121/1.402505.

Brekhovskikh, L.M., 1960. Waves in Layered Media. Academic Press, New York.

Carcione, J.M., 2001. Wave Fields in Real Media: Wave Propagation in Anisotropic, Anelastic and Porous Media. ISSN. Elsevier Science, ISBN: 9780080543710, URL https://books.google.co.il/books?id=feOC0H1m5_wC.

Chaplain, Gregory J., Ponti, Jacopo M. De, Colombi, Andrea, Fuentes-Dominguez, Rafael, Dryburg, Paul, Pieris, Don, Smith, Richard J., Clare, Adam, Clark, Matt, Craster, Richard V., 2020. Tailored elastic surface to body wave umklapp conversion. Nature Commun. 11 (1), 3267. http://dx.doi.org/10.1038/s41467-020-17021-x.

Christensen, J., Willatzen, M., Velasco, V.R., Lu, M.-H., 2016. Parity-time synthetic phononic media. Phys. Rev. Lett. 116 (20), 207601. http://dx.doi.org/10.1103/PhysRevLett.116.207601, URL https://link.aps.org/doi/10.1103/PhysRevLett.116.207601.

Djorwe, P., Pennec, Y., Djafari-Rouhani, B., 2019. Exceptional point enhances sensitivity of optomechanical mass sensors. Phys. Rev. Appl. 12, 024002. http://dx.doi.org/10.1103/PhysRevApplied.12.024002, URL https://link.aps.org/doi/10.1103/PhysRevApplied.12.024002.

Domínguez-Rocha, V., Thevamaran, Ramathasan., Ellis, F.M., Kottos, T., 2020. Environmentally induced exceptional points in elastodynamics. Phys. Rev. A 13, 014060. http://dx.doi.org/10.1103/PhysRevApplied.13.014060, URL https://link.aps.org/doi/10.1103/PhysRevApplied.13.014060.

El-Ganainy, Ramy, Khajavikhan, Mercedeh, Christodoulides, Demetrios N., Ozdemir, Sahin K., 2019. The dawn of non-Hermitian optics. Communications Physics 2 (1), 37. http://dx.doi.org/10.1038/s42005-019-0130-z.

El-Ganainy, Ramy, Makris, Konstantinos G., Khajavikhan, Mercedeh, Musslimani, Ziad H., Rotter, Stefan, Christodoulides, Demetrios N., 2018. Non-Hermitian physics and PT symmetry. Nat. Phys. 14, 11 EP. http://dx.doi.org/10.1038/nphys4323.

Elbaz, Guy, Pick, Adi, Moiseyev, Nimrod, Shmuel, Gal, 2022. Encircling exceptional points of bloch waves: mode conversion and anomalous scattering. J. Phys. D: Appl. Phys. URL http://iopscience.iop.org/article/10.1088/1361-6463/ac5859.

Fang, Yanghao, Kottos, Tsampikos, Thevamaran, Ramathasan, 2021. Universal route for the emergence of exceptional points in pt-symmetric metamaterials with unfolding spectral symmetries. New J. Phys. 23 (6), 063079. http://dx.doi.org/10.1088/1367-2630/ac09c9.

Fang, Yanghao, Kottos, Tsampikos, Thevamaran, Ramathasan, 2022. Emergence of exceptional points in periodic metastructures with hidden parity-time symmetric defects. J. Appl. Mech. (ISSN: 0021-8936) 89 (12), 121003. http://dx.doi.org/10.1115/1.4055618.

Feng, Liang, El-Ganainy, Ramy, Ge, Li, 2017. Non-Hermitian photonics based on parity–time symmetry. Nat. Photonics 11 (12), 752–762. http://dx.doi.org/10.1038/s41566-017-0031-1.

Figotin, A., Vitebskiy, I., 2003. Oblique frozen modes in periodic layered media. Phys. Rev. E 68, 036609. http://dx.doi.org/10.1103/PhysRevE.68.036609, URL https://link.aps.org/doi/10.1103/PhysRevE.68.036609.

Figotin, Alex, Vitebskiy, Ilya, 2006. Slow light in photonic crystals. Waves Random Complex Media 16 (3), 293–382. http://dx.doi.org/10.1080/17455030600836507.

Fleury, Romain, Sounas, Dimitrios L., Alù, Andrea, 2014. Negative refraction and planar focusing based on parity-time symmetric metasurfaces. Phys. Rev. Lett. 113, 023903. http://dx.doi.org/10.1103/PhysRevLett.113.023903, URL https://link.aps.org/doi/10.1103/PhysRevLett.113.023903.

Fleury, Romain, Sounas, Dimitrios, Alù, Andrea, 2015. An invisible acoustic sensor based on parity-time symmetry. Nature Commun. (ISSN: 2041-1723) 6, 5905. http://dx.doi.org/10.1038/ncomms6905, URL http://www.nature.com/doifinder/10.1038/ncomms6905.

Gan, Zhi Ming, Li, Huanan, Kottos, Tsampikos, 2019. Effects of disorder in frozen-mode light. Opt. Lett. 44 (11), 2891–2894. http://dx.doi.org/10.1364/OL.44.002891, URL https://opg.optica.org/ol/abstract.cfm?URI=ol-44-11-2891.

Goldstein, Tal, Shmuel, Gal, 2023. Oblique scattering from non-Hermitian optical waveguides. Phys. Rev. A 107, 023503. http://dx.doi.org/10.1103/PhysRevA.107.023503, URL https://link.aps.org/doi/10.1103/PhysRevA.107.023503.

Guo, Y.Q., Li, Q.Q., Peng, B.R., 2023. Anisotropy and dispersion of elastic waves in periodically multilayered anisotropic media. Compos. Struct. (ISSN: 0263-8223) 324, 117558. http://dx.doi.org/10.1016/j.compstruct.2023.117558, URL https://www.sciencedirect.com/science/article/pii/S0263822323009042.

Gupta, Abhishek, Kurnosov, Arkady, Kottos, Tsampikos, Thevamaran, Ramathasan, 2023. Reconfigurable enhancement of actuation forces by engineered losses in non-Hermitian metamaterials. Extreme Mech. Lett. (ISSN: 2352-4316) 59, 101979. http://dx.doi.org/10.1016/j.eml.2023.101979, URL https://www.sciencedirect.com/science/article/pii/S2352431623000251.

Joseph, L.M., Craster, R.V., 2015. Reflection from a semi-infinite stack of layers using homogenization. Wave Motion (ISSN: 0165-2125) 54, 145–156. http://dx.doi.org/10.1016/j.wavemoti.2014.12.003, URL http://www.sciencedirect.com/science/article/pii/S0165212514001747.

Kato, T., 1966. Perturbation Theory of Linear Operators. Springer, Berlin.

Katsantonis, Ioannis, Droulias, Sotiris, Soukoulis, Costas M., Economou, Eleftherios N., Kafesaki, Maria, 2020. Pt-symmetric chiral metamaterials: Asymmetric effects and pt-phase control. Phys. Rev. B 101 (21), 214109.

Kononchuk, Rodion, Cai, Jizhe, Ellis, Fred, Thevamaran, Ramathasan, Kottos, Tsampikos, 2022. Exceptional-point-based accelerometers with enhanced signal-to-noise ratio. Nature 607 (7920), 697–702. http://dx.doi.org/10.1038/s41586-022-04904-w.

Langley, R.S., 1996. The response of two-dimensional periodic structures to point harmonic forcing. J. Sound Vib. 197 (4), 447–469.

Laude, Vincent, Martínez, Julio Andrés Iglesias, Wang, Yan-Feng, Kadic, Muamer, 2021. Effective anisotropy of periodic acoustic and elastic composites. J. Appl. Phys. (ISSN: 0021-8979) 129 (21), 215106. http://dx.doi.org/10.1063/5.0045827.

Lee, E.H., Yang, Wei H., 1973. On waves in composite materials with periodic structure. SIAM J. Appl. Math. 25 (3), 492–499. http://dx.doi.org/10.1137/0125049.

Lefebvre, G., Antonakakis, T., Achaoui, Y., Craster, R.V., Guenneau, S., Sebbah, P., 2017. Unveiling extreme anisotropy in elastic structured media. Phys. Rev. Lett. 118, 254302. http://dx.doi.org/10.1103/PhysRevLett.118.254302, URL https://link.aps.org/doi/10.1103/PhysRevLett.118.254302.

Li, Huanan, Vitebskiy, Ilya, Kottos, Tsampikos, 2017. Frozen mode regime in finite periodic structures. Phys. Rev. B 96 (18), 180301. http://dx.doi.org/10.1103/PhysRevB.96.180301, URL https://link.aps.org/doi/10.1103/PhysRevB.96.180301.

Lin, Zin, Ramezani, Hamidreza, Eichelkraut, Toni, Kottos, Tsampikos, Cao, Hui, Christodoulides, Demetrios N., 2011. Unidirectional invisibility induced by $\mathcal{PT}$-symmetric periodic structures. Phys. Rev. Lett. 106, 213901. http://dx.doi.org/10.1103/PhysRevLett.106.213901, URL https://link.aps.org/doi/10.1103/PhysRevLett.106.213901.

Longhi, Stefano, 2011. Invisibility in $\mathcal{PT}$-symmetric complex crystals. J. Phys. A 44 (48), 485302. http://dx.doi.org/10.1088/1751-8113/44/48/485302.

Longhi, Stefano, 2017. Parity-time symmetry meets photonics: A new twist in non-Hermitian optics. EPL (Europhys. Lett.) 120 (6), 64001. http://dx.doi.org/10.1209/0295-5075/120/64001.

Lowe, M.J.S., 1995. Matrix techniques for modeling ultrasonic waves in multilayered media. IEEE Trans. Ultrason. Ferroelectr. Freq. Control (ISSN: 0885-3010) 42 (4), 525–542. http://dx.doi.org/10.1109/58.393096.

Lustig, Ben, Elbaz, Guy, Muhafra, Alan, Shmuel, Gal, 2019. Anomalous energy transport in laminates with exceptional points. J. Mech. Phys. Solids (ISSN: 0022-5096) 103719. http://dx.doi.org/10.1016/j.jmps.2019.103719, URL http://www.sciencedirect.com/science/article/pii/S0022509619306921.

Merkel, Aurélien, Romero-García, Vicent, Groby, Jean-Philippe, Li, Jensen, Christensen, Johan, 2018. Unidirectional zero sonic reflection in passive $\mathcal{PT}$-symmetric Willis media. Phys. Rev. B 98, 201102. http://dx.doi.org/10.1103/PhysRevB.98.201102, URL https://link.aps.org/doi/10.1103/PhysRevB.98.201102.

Midya, Bikashkali, Zhao, Han, Feng, Liang, 2018. Non-Hermitian photonics promises exceptional topology of light. Nature Commun. 9 (1), 2674. http://dx.doi.org/10.1038/s41467-018-05175-8.

Miri, Mohammad-Ali, Alù, Andrea, 2019. Exceptional points in optics and photonics. Science (ISSN: 0036-8075) 363 (6422), http://dx.doi.org/10.1126/science.aar7709, URL https://science.sciencemag.org/content/363/6422/eaar7709.

Moiseyev, Nimrod, 2011. Non-Hermitian Quantum Mechanics. Cambridge University Press, http://dx.doi.org/10.1017/CBO9780511976186.

Mokhtari, Amir Ashkan, Lu, Yan, Srivastava, Ankit, 2019. On the properties of phononic eigenvalue problems. J. Mech. Phys. Solids (ISSN: 0022-5096) http://dx.doi.org/10.1016/j.jmps.2019.07.005, URL http://www.sciencedirect.com/science/article/pii/S0022509619304247.

Mokhtari, Amir Ashkan, Lu, Yan, Zhou, Qiyuan, Amirkhizi, Alireza V., Srivastava, Ankit, 2020. Scattering of in-plane elastic waves at metamaterial interfaces. Internat. J. Engrg. Sci. (ISSN: 0020-7225) 150, 103278. http://dx.doi.org/10.1016/j.ijengsci.2020.103278, URL https://www.sciencedirect.com/science/article/pii/S0020722520300665.

Nada, Mohamed Y., Mealy, Tarek, Capolino, Filippo, 2021. Frozen mode in three-way periodic microstrip coupled waveguide. IEEE Microw. Wirel. Compon. Lett. 31 (3), 229–232. http://dx.doi.org/10.1109/LMWC.2020.3042205.

Nayfeh, Adnan H., 1991. The general problem of elastic wave propagation in multilayered anisotropic media. J. Acoust. Soc. Am. (ISSN: 0001-4966) 89 (4), 1521–1531. http://dx.doi.org/10.1121/1.400988.

Nayfeh, A.H., 1995. Wave Propagation in Layered Anisotropic Media: With Application to Composites. In: North-Holland Series in Applied Mathematics and Mechanics, Elsevier Science, ISBN: 9780444890184, URL https://books.google.co.il/books?id=8p4eAQAAIAAJ.

Özdemir, Ş.K., Rotter, S., Nori, F., Yang, L., 2019. Parity–time symmetry and exceptional points in photonics. Nature Mater. 18 (8), 783–798. http://dx.doi.org/10.1038/s41563-019-0304-9.

Psiachos, D., Sigalas, M.M., 2019. Tailoring one-dimensional layered metamaterials to achieve unidirectional transmission and reflection. Phys. Rev. B (ISSN: 2469-9950) 99 (18), http://dx.doi.org/10.1103/PhysRevB.99.184110.

Romeo, Francesco, Luongo, Angelo, 2002. Invariant representation of propagation properties for bi-coupled periodic structures. J. Sound Vib. 257 (5), 869–886.

Rosa, Matheus I.N., Mazzotti, Matteo, Ruzzene, Massimo, 2021. Exceptional points and enhanced sensitivity in pt-symmetric continuous elastic media. J. Mech. Phys. Solids (ISSN: 0022-5096) 149, 104325. http://dx.doi.org/10.1016/j.jmps.2021.104325, URL https://www.sciencedirect.com/science/article/pii/S0022509621000314.

Shi, Chengzhi, Dubois, Marc, Chen, Yun, Cheng, Lei, Ramezani, Hamidreza, Wang, Yuan, Zhang, Xiang, 2016. Accessing the exceptional points of parity-time symmetric acoustics. Nat. Commun. 7, 11110.

Shmuel, Gal, Moiseyev, Nimrod, 2020. Linking scalar elastodynamics and non-Hermitian quantum mechanics. Phys. Rev. Appl. 13, 024074. http://dx.doi.org/10.1103/PhysRevApplied.13.024074, URL https://link.aps.org/doi/10.1103/PhysRevApplied.13.024074.

Srikantha Phani, A., 2022. Dissipation driven degeneracies. Appl. Phys. Lett. (ISSN: 0003-6951) 121 (23), 231701. http://dx.doi.org/10.1063/5.0118099.

Srivastava, A., 2016. Metamaterial properties of periodic laminates. J. Mech. Phys. Solids (ISSN: 0022-5096) 96, 252–263. http://dx.doi.org/10.1016/j.jmps.2016.07.018, URL http://www.sciencedirect.com/science/article/pii/S0022509616303933.

Srivastava, A., Willis, J.R., 2017. Evanescent wave boundary layers in metamaterials and sidestepping them through a variational approach. Proc. R. Soc. London A Math. Phys. Eng. Sci. (ISSN: 1364-5021) 473 (2200), http://dx.doi.org/10.1098/rspa.2016.0765, URL http://rspa.royalsocietypublishing.org/content/473/2200/20160765.

Stroh, A.N., 1962. Steady state problems in anisotropic elasticity. J. Math. Phys. 41 (1–4), 77–103. http://dx.doi.org/10.1002/sapm196241177, URL https://onlinelibrary.wiley.com/doi/abs/10.1002/sapm196241177.

Suntharalingam, Arunn, Fernández-Alcázar, Lucas, Kononchuk, Rodion, Kottos, Tsampikos, 2023. Noise resilient exceptional-point voltmeters enabled by oscillation quenching phenomena. Nature Commun. 14 (1), 5515. http://dx.doi.org/10.1038/s41467-023-41189-7.

Sweeney, William R., Hsu, Chia Wei, Rotter, Stefan, Douglas Stone, A., 2019. Perfectly absorbing exceptional points and chiral absorbers. Phys. Rev. Lett. 122, 093901. http://dx.doi.org/10.1103/PhysRevLett.122.093901, URL https://link.aps.org/doi/10.1103/PhysRevLett.122.093901.

Tuxbury, W., Fernandez-Alcazar, L.J., Vitebskiy, I., Kottos, T., 2021. Scaling theory of absorption in the frozen mode regime. Opt. Lett. 46 (13), 3053–3056, URL https://opg.optica.org/ol/abstract.cfm?URI=ol-46-13-3053.

Tuxbury, William, Kononchuk, Rodion, Kottos, Tsampikos, 2022. Non-resonant exceptional points as enablers of noise-resilient sensors. Commun. Phys. 5 (1), 210. http://dx.doi.org/10.1038/s42005-022-00973-5.

Wang, Weidi, Amirkhizi, Alireza V., 2022. Exceptional points and scattering of discrete mechanical metamaterials. Eur. Phys. J. Plus 137 (4), 414. http://dx.doi.org/10.1140/epjp/s13360-022-02626-6.

Wang, Changqing, Sweeney, William R., Douglas Stone, A., Yang, Lan, 2021. Coherent perfect absorption at an exceptional point. Science 373 (6560), 1261–1265. http://dx.doi.org/10.1126/science.abj1028, URL https://www.science.org/doi/abs/10.1126/science.abj1028.

Wiersig, Jan, 2014. Enhancing the sensitivity of frequency and energy splitting detection by using exceptional points: Application to microcavity sensors for single-particle detection. Phys. Rev. Lett. 112, 203901. http://dx.doi.org/10.1103/PhysRevLett.112.203901, URL https://link.aps.org/doi/10.1103/PhysRevLett.112.203901.

Willis, J.R., 2015. Negative refraction in a laminate. J. Mech. Phys. Solids (ISSN: 0022-5096) 97, 10–18. http://dx.doi.org/10.1016/j.jmps.2015.11.004, URL http://www.sciencedirect.com/science/article/pii/S0022509615302623.

Zamir-Abramovich, Kessem, Furman, Nathaniel, Herrero-Parareda, Albert, Capolino, Filippo, Scheuer, Jacob, 2023. Low-threshold lasing with frozen mode regime and stationary inflection point in three coupled waveguide structure. arXiv.